Journal of Materials Science: Materials in Electronics (2020) 31:15286–15295
https://doi.org/10.1007/s10854-020-04093-0

Enhancing the electrochemical and cyclic performance of IRFBs through electrode modification using novel $MnO_2@CeO_2$ composite

M. S. Anantha[1,2] · **D. Anarghya**[1,2] · **Chunyan Hu**[3,4] · **Narendra Reddy**[1] · **Krishna Venkatesh**[1] · **H. B. Muralidhara**[1]

Received: 21 May 2020 / Revised: 11 July 2020 / Accepted: 23 July 2020 / Published online: 31 July 2020

Abstract

In this work, we have coated $MnO_2@CeO_2$ composites onto graphite felts (GF) by electrostatic spraying leading to substantially improved electrochemical performance characteristics of iron redox flow batteries. GF are extensively used as electrodes but they do not have the desired electrochemical properties. $MnO_2@CeO_2$ composites have novel electrocatalyst features. Hence, $MnO_2@CeO_2$ composites were developed and applied to GF. Chemical and structural features of the bare graphite felt electrode and $MnO_2@CeO_2$ composite-modified graphite felt electrode (MGF) were characterized using scanning electron microscopy, energy dispersive X-ray analysis, transmission electron microscopy, X-ray diffraction, and Brunauer–Emmett–Teller surface area analysis. Similarly, the electrochemical performance was investigated using cyclic voltammetry, electrochemical impedance spectroscopy, Tafel, and charge–discharge performance experiments. The charge–discharge experiments were performed at 1 to 3 mg cm^{-2} weight of MGFs and varying the current densities from 40 to 70 mA cm^{-2}. The coulombic efficiency (η_C) and peak power density (PPD) of the cell (132 cm^2) determined at 50 mA cm^{-2} for 2 mg cm^{-2}-MGF electrode was found to be 99.10% and 55.56 W cm^{-2}, respectively. Among the three different types of electrodes, the MGF electrode showed better electrocatalytic performance mainly due to the excellent conducting network of the oxygen moieties of $MnO_2@CeO_2$ composites. After 25 cycles, the average η_C and PPD of the cell using 2 mg cm^{-2}-MGF was found to be 96.06% and 55.16 mW cm^{-2}, respectively, indicating the good stability of the electrode.

1 Introduction

Since the last decade, nanomaterials have played a critical role in developing new technologies to generate energy and also in devising novel energy storage devices. However, properties of nanomaterials are directly dependent on polymorphism, morphology, size of particles, size distribution, presence of external coatings, and the type of precursor used in the synthesis [1]. Nano-based materials have been extensively considered to develop new energy systems, specifically for renewable energy storage and conversion. Large-scale energy storage devices [2], such as Li-ion [3], Na–S [4], and redox flow batteries (RFBs) [2] have evolved to promote renewable energy generation and storage. Among the unique storage devices, iron redox flow batteries (IRFBs) are suggested to be most promising for large-scale energy storage due to their long cycle life, charge–discharge capabilities, and flexible design. Similarly, carbon-based materials, such as graphite felts (GF) are preferred as electrodes in IRFBs, due to their excellent strength, high electrical conductivity, porous structure, and acid resistance [5]. However, the poor electrocatalytic activity of IRFBs decreases the capacity and lowers the efficiency at higher current densities, thereby preventing their wider application and large-scale commercialization. Enhancing the wide energetic active sites on the surface of GF electrode used in IRFBs and introducing additional functional groups are considered effective to overcome the limitations [5, 6].

✉ H. B. Muralidhara
hb.murali@gmail.com

[1] Centre for Incubation, Innovation, Research and Consultancy (CIIRC), Jyothy Institute of Technology, Thataguni, Off Kanakapura Road, Bangalore, Karnataka 560 082, India

[2] Research Resource Centre, Visvesvaraya Technological University, Jnana sangama, Belagavi, Karnataka 590018, India

[3] College of Chemistry, Chemical Engineering and Biotechnology, Donghua University, Shanghai 201620, People's Republic of China

[4] National Engineering Research Center for Dyeing and Finishing of Textiles, Donghua University, Shanghai 201620, People's Republic of China

IRFBs are taken into consideration to be efficient for grid-level storage. In IRFBs, Fe^{2+}/Fe^{3+} and Fe^{2+}/Fe act as positive and negative electrolytes, respectively. A typical reaction occurring in the IRFBs is given in Equations 1–3 listed below:

$$2Fe^{2+} \leftrightarrow 2Fe^{3+} + 2e^{-} E^{0} = 0.77V \text{ vs. NHE} \tag{1}$$

$$Fe^{2+} + 2e^{-} \leftrightarrow Fe^{0} E^{0} = -0.44V \text{ vs. NHE} \tag{2}$$

$$3Fe^{2+} \leftrightarrow Fe^{0} + 2Fe^{3+} E^{0} = 1.21 \text{ vs. NHE} \tag{3}$$

Electrodes are the essential components in any RFB systems [7] which in turn are dependent on the composition, structure, and performance of the materials used to develop the electrodes. The performance and efficiency of batteries are directly related to the performance of the electrodes. Hence, considerable attention has been given to develop appropriate electrodes or modify the electrodes to achieve the desired battery performance. Among the different materials used to modify the electrodes metal oxides, rare earth oxides, carbon catalysts, functionalized organic materials, heteroatom-doped catalysts are common. These materials act as electrocatalysts in the modified electrodes and increase the effectiveness of redox reactions by exchanging ions and charges.

The electrochemical activity and cyclic stability of IRFBs may be improved by the usage of many noble metals (Pt, Ir, Ru, Au, Pd, etc.) [8, 9]. Such metals have been deposited on the surfaces of GF by the use of numerous techniques. For instance, an increase in electrochemically actives sites on the surface of GF and reduction in the resistance of the GF lead to improved electrical conductivity in the IRFBs. However, metals on GF are affected by the gases released during the redox reactions occurring in IRFBs. The process of deposition of metals also makes the GF expensive. Several studies have been done to develop low-cost metals and carbon-based catalysts with higher electrocatalytic performance. Instead of noble metals, inexpensive metals and metal oxides (Mn_3O_4, CeO_2, WO_3, Ti, W, Ni) [10–14] have additionally been used to enhance the electrochemical reactions, but their catalytic activity largely relies upon the scale and stability of the catalysts on the surface of the GF. Therefore, a combination of metal and metal oxide nanocomposites could enhance the electrochemical activity and stability [14]. It is critical to design nanomaterial-based electrocatalysts that are non-toxic, inexpensive, and provide good electrochemical performance and stability to ensure large-scale energy storage devices like IRFBs are not only efficient but also cost-effective and suitable for large-scale energy storage.

Among the various oxides used, cerium oxide (CeO_2) with a bandgap of 2.58 eV has gained significance because of its excellent properties like electrocatalytic activity, high oxygen storage capacity, and low energy barrier among III and IV oxidation states [15]. These unique features help to advance the applications of CeO_2 for hydrogen generation [16], solar cells [17], environmental remediation [18], oxidation of CO [19], and in developing supercapacitors with high specific capacity [20] or as cathode/anode component in RFBs [21–23]. CeO_2 when used for electrode modification shows a significant improvement in the cyclic stability and retention capacity of lithium-ion batteries [24]. It should be noted that integrating a proper co-catalyst with an active catalyst to form a heterojunction is an effective method for enhancing electrocatalytical performance [25, 26]. MnO_2 as an electrocatalytically active material shows good electrical conductivity, unique catalytic redox ability, and generation of large amounts of surface oxygen species. Recently, reduced graphene oxide@MnO_2 [27] and BiOI/MnO_2 [28] composite semiconductors were constructed with an inclusive heterojunction of the MnO_2 as an active material. However, the prepared heterojunctions based on MnO_2 have limitations in terms of complex processes and high cost. During the development of MnO_2-based heterojunctions, the addition of a reducing agent (carbon), which is synthesized using organic matter by carbonization [29, 30] is necessary. Considering the overall aspects, CeO_2 and MnO_2 justify the synthesis of MnO_2@CeO_2 heterostructure but a relatively simple and cost-effective process should be developed. The heterostructure was formed by the overlapping of MnO_2 particles on the surface of CeO_2 particle to provide an efficient electrocatalytic activity for further modification of the GF and to enhance the charge/discharge and cycle stability of the IRFBs.

Herein, novel MnO_2@CeO_2 composites containing oxygen moieties having porous spherical and dry leaf stick morphology have been developed. MnO_2@CeO_2 composite was first fabricated on the surface of the GF to increase the electrocatalytic activity. Later, MnO_2@CeO_2 composite-modified graphite felt electrodes (MGF) were used to increase the performance of IRFBs. The proposed MnO_2@CeO_2 composite structure and its properties effectively improve the iron redox reactions in the IRFBs. An increase in the electrochemical performance and cyclic stability of the MGF was possible and hence, the proposed strategy has great potential for applications in IRFBs.

2 Materials and methods

2.1 Materials

Raw materials used in the experiments include cerium nitrate hexahydrate ($Ce(NO_3)_3 \cdot 6H_2O$), urea ($CO(NH_2)_2$), potassium permanganate ($KMnO_4$), manganous sulfate ($MnSO_4 \cdot H_2O$), ferrous chloride ($FeCl_2$), glycine ($C_2H_5NO_2$), ammonium chloride (NH_4Cl), and Ethanol (C_2H_5OH) (Analytical reagents, AR) which were procured from Bangalore Scientific and Industrial Supplies, Bangalore, India. All chemicals were used as received, without further purifications. The graphite felt electrode was procured from Rayon Graphite felt (AGFHT), USA. The anionic membrane (FUMASEP FAP-375PP) and Nafion binder used were obtained from Fuel Cell Store, USA. The battery components such as reinforced epoxy end plates of 15 mm thickness, copper plates, and gaskets were fabricated in-house, graphite serpentine flow fields were machined with the help of a local vendor M/s Mersen India Pvt Ltd., Bangalore. A schematic of the battery components and assembled system is shown in Scheme 1.

2.2 Preparation of MnO_2@CeO_2 composite

Precisely 0.26 g of Ce $(NO_3)_3.6H_2O$ and 2.25 g of CO $(NH_2)_2$ were dissolved in 60 ml of deionized water under stirring at 200 rpm in a beaker. In separate beakers, 0.448 g of $MnSO_4{\cdot}H_2O$ and 1.0 g of $KMnO_4$ were dissolved in 30 ml of deionized water separately. The $MnSO_4{\cdot}H_2O$ solution was transferred into $KMnO_4$ solution and the two solutions were mixed thoroughly for about 30 min. Later, the mixed solution was transferred into a stainless steel autoclave, and the temperature was raised to 433 K and maintained for 24 h. After the reaction terminated, the solution was allowed to cool down to room temperature. The brownish precipitate formed was removed from the solution by centrifugation at 8000 rpm and the collected material was washed with deionized water until the water became colorless. The prepared product was dried at 333 K for 12 h, and calcined at 573 K for 3 h in a muffle furnace. The final powder having brownish color was stored in an airtight container [20].

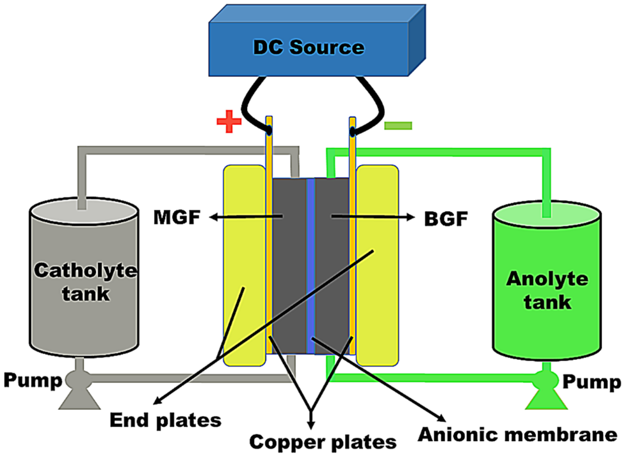

Scheme 1 A typical assembly of the IRFBs

2.3 Modification of bare graphite felt electrode (BGF)

A known quantity of MnO_2@CeO_2 composite was dispersed in alcohol by continuous stirring at 350 rpm for about 5 h at room temperature. Nafion (5 wt%) was added to the above solution and sonicated for about 15 min. Later, either side of the BGF was coated with MnO_2@CeO_2 composite using a nozzle spray gun (Aimex H-827) having 1.4 mm internal diameter and operating at an air pressure of 58 PSI. Coated electrodes were vacuum dried for about 24 h at 353 K and 25 PSI.

2.4 Characterization

The prepared material was subject to extensive testing and characterizations. The morphological study of the MnO_2@CeO_2 composite, BGF and MGF were conducted using SEM (HITACHI, SU3500) equipped with an EDAX system. TEM analysis was done by Philips CM-200. XRD investigations were conducted on BRUKER eco-D8 ADVANCE diffractometer working with CuKα radiation ($\lambda = 1.54$ Å). Raman spectra of BGF and MGF were analyzed using (HORIBA-JOBINYVON, LABRAM) with 532 nm LASER at an exposure time of 5 s. Charge-coupled device (CCD) was used as detector for the analysis with 1800 lines/mm grating. Determination of specific surface area, pore volume, and pore diameter was done on ASAP 2010 Micrometrics instrument.

2.5 Electrochemical studies

Cyclic voltammetry (CV), Electrochemical Impedance Spectroscopy (EIS, frequency range: 0.01 to 10^5 Hz), and Tafel analysis were carried out using an electrochemical work station (CHI600E Series) with the conventional three-electrode system. The working electrodes used in the study were BGF, MGFs. An Ag/AgCl electrode was used as the reference electrode and platinum was the counter electrode. $FeCl_2$ solution was prepared using deionized water and used as the electrolyte. All the experiments were performed under ambient temperature.

2.6 Charge–discharge studies

A single-cell having 132 cm^2 active area with MGF and BGF as positive and negative electrodes, respectively, were used for the charge–discharge studies (Fig. 1). FUMASEP FAP-375PP was used as a separator.

The iron electrolyte was prepared using a mixture of 3.25 m $FeCl_2$, 0.3 m $C_2H_5NO_2$, and 1.0 m NH_4Cl in deionized water. Here, $C_2H_5NO_2$ acts as ligand and reduces the pH imbalance of the electrolytes. NH_4Cl increases the conductivity of the $FeCl_2$ electrolyte. The iron electrolyte

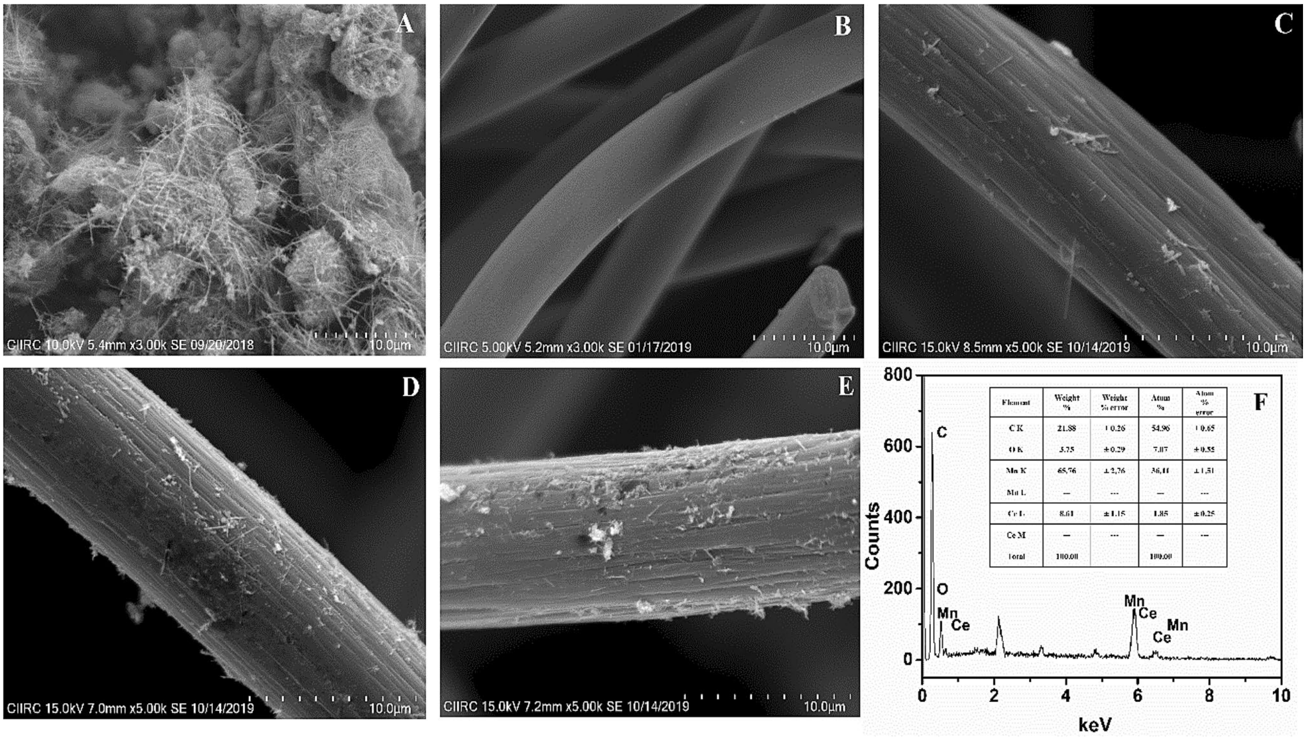

Element	Weight %	Weight % error	Atom %	Atom % error
C K	21.88	±0.26	54.96	±0.65
O K	3.75	±0.29	7.07	±0.55
Mn K	65,76	±2,76	36,11	±1,51
Mn L	—	---	—	---
Ce L	8.61	±1.15	1.85	±0.25
Ce M	—	---	—	---
Total	100.00		100.00	

Fig. 1 SEM images of **a** $MnO_2@CeO_2$ composite, **b** BGF electrode, **c** 1 mg cm^{-2}-MGF electrode, **d** 2 mg cm^{-2}-MGF electrode, **e** 3 mg cm^{-2}-MGF electrode, **f** EDAX of 2 mg cm^{-2}-MGF electrode

which is stored in glass reservoirs and acts as anolyte and catholyte was connected to the redox flow cell using a rubber hose. The flow of the electrolyte into the cell was controlled at 130 ml min^{-1} using a peristaltic pump (RH-P100L-200-2 h-1D). The charge–discharge and cycling analysis were performed using a Bitrode life cycle tester (LCV4-100/1–48) by varying the current density from 10 to 50 mA cm^{-2} and potential between 0.8 and 1.5 V.

Coulombic efficiency (η_C) was calculated using the following equation:

$$\text{Coulombic efficiency} = \frac{\text{Discharge current} \times \text{Discharge time}}{\text{Charge current} \times \text{Charge time}} \times 100 \tag{4}$$

3 Results and discussion

3.1 Morphological and structural analysis

Figure 1 shows the SEM analysis of the $MnO_2@CeO_2$ composite, BGF and MGFs and EDAX of the MGF. The morphology of the composite consists of a combination of dry leaves sticks and spherical dust nanoaggregate-like particles as seen from Fig. 1a. Figure 1b represents the microwire morphology of BGF electrode with clean surface. Figures 1c–e show SEM images of the MGF electrodes with an increasing weight of the $MnO_2@CeO_2$ composite particles from 1 to 3 mg cm^{-2}. The dry leaf sticks and dust nanoaggregate-like particles were uniformly deposited on the surface of the GF electrodes. The deposited $MnO_2@CeO_2$ composites are porous, have sharp edges, and are unique in structure. Such morphology helps the composite to have more active sites of oxygenated moieties, which are responsible for the enhancement of electrocatalytic activity in 2 mg cm^{-2}-MGF electrode. The EDAX results (Fig. 1f) show that the $MnO_2@CeO_2$ composite does not contain any impurities.

TEM images of $MnO_2@CeO_2$ composite at different magnifications are shown in Fig. 2a–c. The composite particles are in nanoscale and their surface is porous as seen from Fig. 2c. The porous structure may have been formed due to the presence of oxygen in the composite moiety. The images also reveal the presence of actives sites on the surface as observed (Fig. 2b) through the overlapping of particles of MnO_2 on the CeO_2 particles (Fig. 2a). $MnO_2@CeO_2$ composites have more active surface for the catalytic performance of the composite in electrochemical applications [31].

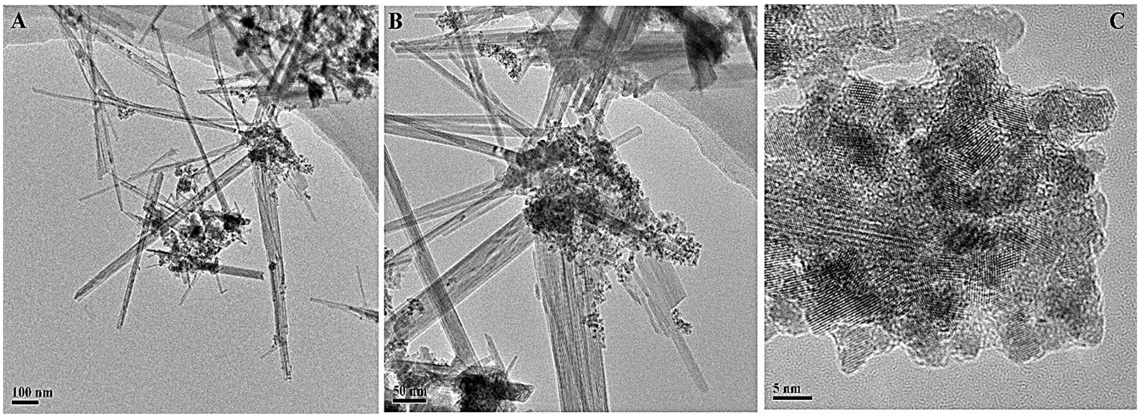

Fig. 2 TEM images of MnO_2@CeO_2 composite at different magnifications **a** 100 nm **b** 50 nm **c** 5 nm

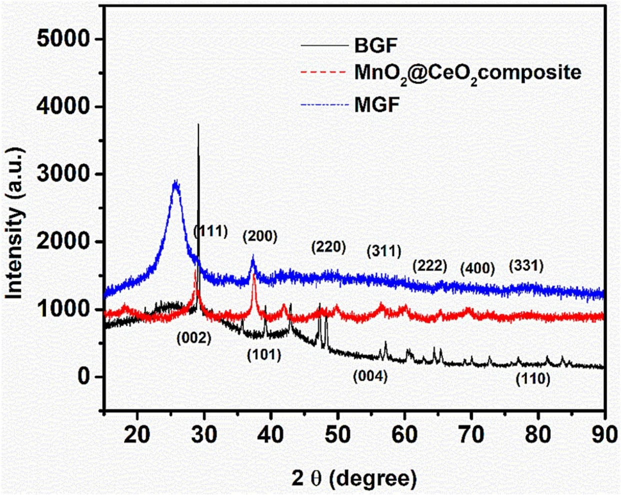

Fig. 3 XRD spectra of pure MnO_2@CeO_2 composite, and BGF and MGF electrodes

Figure 3 shows the XRD diffractograms of MnO_2@CeO_2 composite, and BGF and MGF electrodes. MnO_2@CeO_2 composite exhibits a single crystalline peak which crystallized into a characteristic cubic-type lattice and the lattice constants are consistent with the standard JCPDS (Card No. 00-064-0204) with diffraction peaks at 2θ of 28.75°, 37.44°, 47.13°, 56.43°, 60.07°, 69.17°, and 76.85° corresponding to the diffraction planes of (111), (200), (220), (311), (222), (400), and (331), respectively. MnO_2@CeO_2 composite crystals had all the characteristic diffraction peaks when compared with the standard, thus indicating that the MnO_2@CeO_2 composite crystals were grown in all orientations. Upon comparison with the standard file, MnO_2@CeO_2 composite indicated that Mn ions occupy a position within a cubic lattice of ceria with centrosymmetric crystals belonging to Fm-3 m (225) point group [32]. The crystalline phases of BGF and MGF show diffraction peaks at 25.31°, 42.59°, 52.59°, and 77.98° representing the hkl planes (002), (101), (004), and (110), respectively. The intensity of the peaks broadens and the peaks shift in the MGF which was also observed in BGF electrode and MnO_2@CeO_2 composite, due to the oxidation of the BGF due to thermal exposure during drying or depositing the MnO_2@CeO_2 composite. Using Scherrer's equation, the average crystal size of composite particle was determined to be 7.62 nm.

$$D = \frac{0.9\lambda}{\beta\cos\theta}, \tag{5}$$

where λ is the wavelength of X-rays used (0.154 nm), θ is the Bragg diffraction angle, and β is the full width at half maximum of the XRD pattern of (111) plane.

3.2 BET surface analysis

The adsorption–desorption isotherms and pore distribution curves for MnO_2@CeO_2 composite obtained from the BET analysis in N_2 atmosphere are given in Fig. 4. The adsorption–desorption isotherm plot of relative pressure scale was from 0.50 to 0.99 representing a type IV monolayer formation together with hysteresis loops of type H3. MnO_2@CeO_2 composites shapes were porous slit or plate, in the form of non-rigid aggregates of the type H3, confirming the mesoporous structure of MnO_2@CeO_2 composite particle. The size of the particle was in the range of 2–50 nm which confirms the crystal size of 7.26 nm obtained from the XRD analysis using Scherrer's equation. The pore size of the mesoporous structure of composite particle was between 1 and 3 nm and porosity was 0.219 cc g^{-1}. The developed MnO_2@CeO_2 composite had 99.427 $m^2\ g^{-1}$ of the BET

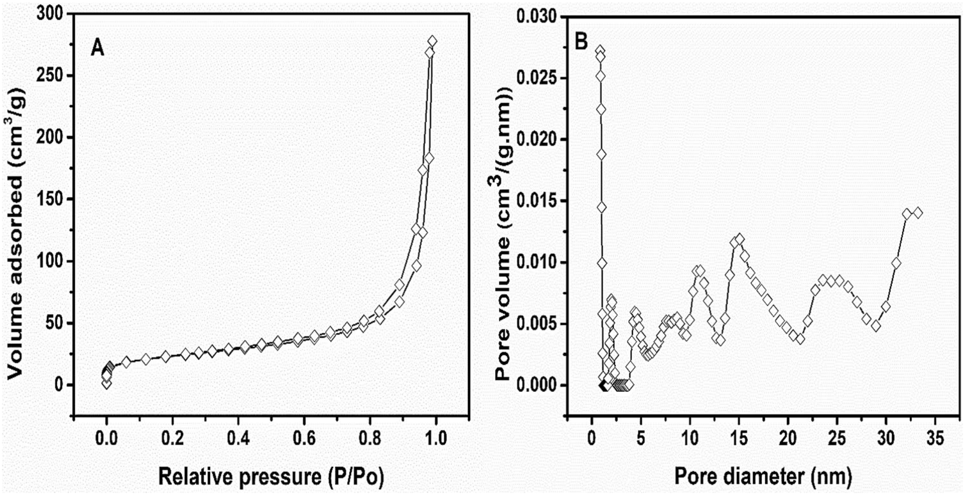

Fig. 4 **a** Nitrogen adsorption–desorption isotherms and **b** corresponding pore size distribution curves of the $MnO_2@CeO_2$ composite

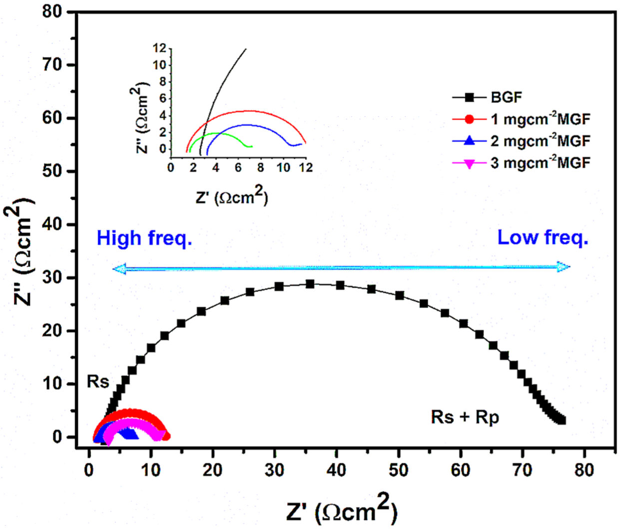

Fig. 5 Electrochemical impedance spectra of BGF and MGF electrodes

Table 1 Parameters obtained by fitting the Nyquist plots

Material	R_s (Ω)	R_p (Ω)
BGF	2.49	76.23
1 mg cm^{-2}-MGF	1.42	12.32
2 mg cm^{-2}-MGF	1.69	6.63
3 mg cm^{-2}-MGF	1.71	16.46

surface area. With the presence of a larger surface area and uniform size of fine nanoparticles, the composites may provide good electrocatalytical performance.

3.3 Electrochemical analysis

EIS measurements were carried out for BGF and MGF electrodes in $FeCl_2$ electrolyte and the results are shown in Fig. 5. The spectra obtained show a similar pattern of depressed capacitive semi-circle in the high-frequency region, whereas a sloping straight line in the low-frequency region. R_s is bulk solution resistance and R_p is Faradaic interfacial charge-transfer resistance which are important parameters indicating the capacity of the electrolyte and working electrodes. R_s and R_p of BGF and MGF electrodes are listed in Table 1. The R_s of all the electrodes were around 1.5 Ω, except BGF which has a considerably higher R_s of 2.49 Ω. The R_p value of BGF was 76.23 Ω, which may be the presence of inactive sites on the surface or due to high internal resistance. The 2 mg cm^{-2}-MGF electrode provides the least R_p value of 2.06 Ω, which may be due to the presence of oxygen moieties within the $MnO_2@CeO_2$ composite and on the surface of the electrodes. The oxygen-active sites enhance the redox reaction of the $FeCl_2$ electrolyte at the interface of the electrode. The resistance of MGF was lowest up to a certain extent of modification, beyond which the resistance increases due to the increase in the internal resistance of $MnO_2@CeO_2$ composite.

The CVs of BGF and GOMGF electrodes are shown in Fig. 6a. 2 mg cm^{-2}-MGF electrode showed a significant difference in the redox peaks compared to BGF electrode. Among all modified electrodes, 2 mg cm^{-2}-MGF electrode exhibits the highest level of electrochemical performance. The relative CV which represents the difference of cathodic and anodic peak potential (ΔE) for 2 mg cm^{-2}-MGF electrode is around 0.203 V at a scan rate of 50 mV s^{-1} compared to BGF and MGF electrodes. Similarly, the ratio of anodic (I_{pa}) and cathodic (I_{pc}) peak current densities is 1.131 which means considerably higher ΔE than the BGF 0.365 V, the relative I_{pa}/I_{pc} is 1.409 which indicates irreversible

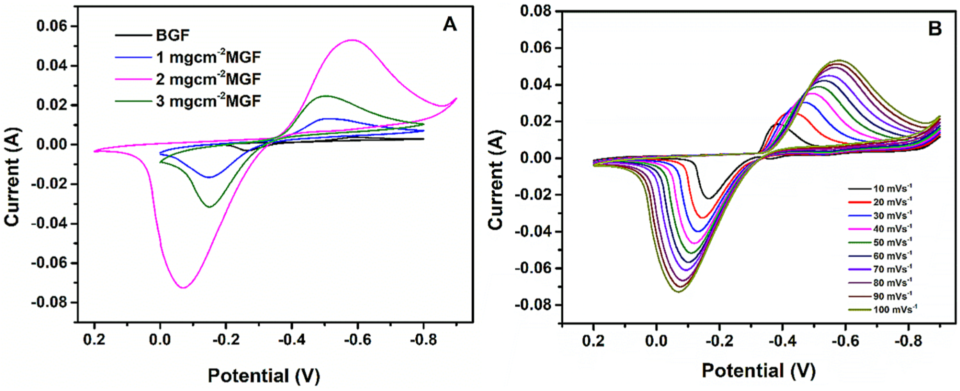

Fig. 6 **a** Cyclic voltammograms on different electrodes in $FeCl_2$ electrolyte at a scan rate of 50 mV s^{-1} and **b** variation of scan rates at 2 mg cm^{-2}-MGF electrode

Table 2 Electrochemical parameters obtained from CV curves

Electrode	I_{pa} (mA cm^{-2})	I_{pc} (mA cm^{-2})	I_{pa}/I_{pc}	E_c (V)	E_a (V)	ΔE (V)
BGF	4.132^{-3}	$2.931e^{-3}$	1.409	0.180	0.545	0.365
1 mg cm^{-2}-MGF	$2.415e^{-3}$	$1.591e^{-3}$	1.517	0.270	0.566	0.296
2 mg cm^{-2}-MGF	$1.991e^{-2}$	$1.759e^{-2}$	1.131	0.260	0.463	0.203
3 mg cm^{-2}-MGF	$5.265e^{-3}$	$7.113e^{-3}$	0.740	0.196	0.500	0.304

reactions towards the Fe^{2+}/Fe^{3+} redox process. The derived electrochemical data are given in Table 2. The lower ΔE and ratio of I_{pa} and I_{pc} approaching 1 in 2 mg cm^{-2}-MGF electrode represent better reversibility and good electrochemical catalytic activity towards Fe^{2+}/Fe^{3+} redox reactions. Figure 6b shows the CV variations as the scan rate changes from 10 mV s^{-1} to 100 mV s^{-1}. The 2 mg cm^{-2}-MGF electrode exhibits the best reversibility and electrochemical catalytic activity. The CV studies have good agreement with the EIS analysis of BGF and MGF electrodes (weight cm^{-2}) based on the ΔE and I_{pa}/I_{pc} values.

Tafel plot of BGF and MGF electrodes is shown in Fig. 7. The linear polarization resistance values calculated from the Tafel plot are given in Table 3. The calculated linear polarization resistance decreases for the BGF, 1 and 2 mg cm^{-2}-MGF electrodes, but the 3 mg cm^{-2}-MGF electrode showed sudden increase in the linear polarization resistance. Among all electrodes, 2 mg cm^{-2}-MGF electrode provides a very low resistance of 5 ohms, whereas 3 mg cm^{-2}-MGF electrode shows a much higher resistance of 59 ohms, which may be due to the increase in internal resistance because of high amount of $MnO_2@CeO_2$ composite on GF electrode. In 3 mg cm^{-2}-MGF electrode, there are higher amount of $MnO_2@CeO_2$ composite particles as observed from the SEM images (Fig. 1e). The lower linear polarization resistance of MGF may also contribute to the high electrocatalytic activity and leads to the deposition of $MnO_2@CeO_2$ composite on the GF electrode.

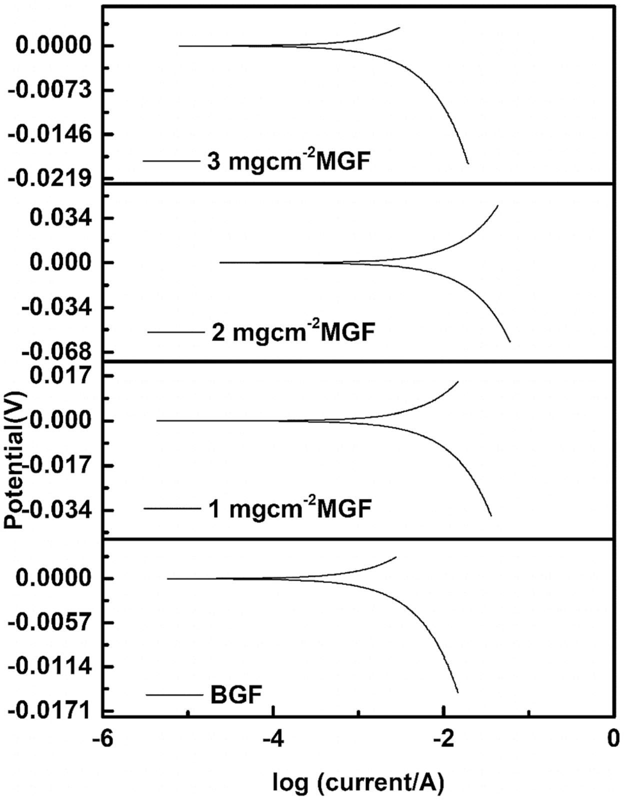

Fig. 7 Tafel plot of BGF and MGF electrodes

Table 3 The linear polarization resistance value of the electrodes from the Tafel plot

Sample	Linear polarization resistance (Ω)
BGF	87
1 mg cm^{-2}-MGF	22
2 mg cm^{-2}-MGF	05
3 mg cm^{-2}-MGF	59

3.4 Performance characterization of single-cell flow battery

The charge–discharge studies were carried out using 132 cm^2 cell between current density of 40 and 70 mA cm^{-2} with C2 rating. In the cell, BGF and MGF electrodes were used as positive electrodes and BGF as a negative electrode. The efficiencies of the cell using MGF electrodes were calculated and compared at 50 mA cm^{-2}. However, BGF electrode exhibits poor electrochemical performance and charge–discharge studies were limited to 20 mA cm^{-2} as indicated in Fig. 8a. The 2 mg cm^{-2}-MGF electrode provides the best efficiencies (98.96%) than the BGF and other MGF electrodes as shown in Fig. 8b. The corresponding η_C and PPD are provided in Table 4. The 2 mg cm^{-2}-MGF electrode shows good reversibility for the redox process for the $FeCl_2$ system (Fe^{2+}/Fe^{3+}), due to the lower charge-transfer resistance and lesser electrochemical polarization as evident in the electrochemical studies.

Figure 8c represents the performance of 2 mg cm^{-2}-MGF electrode at current densities between 40 and 70 mA cm^{-2}.

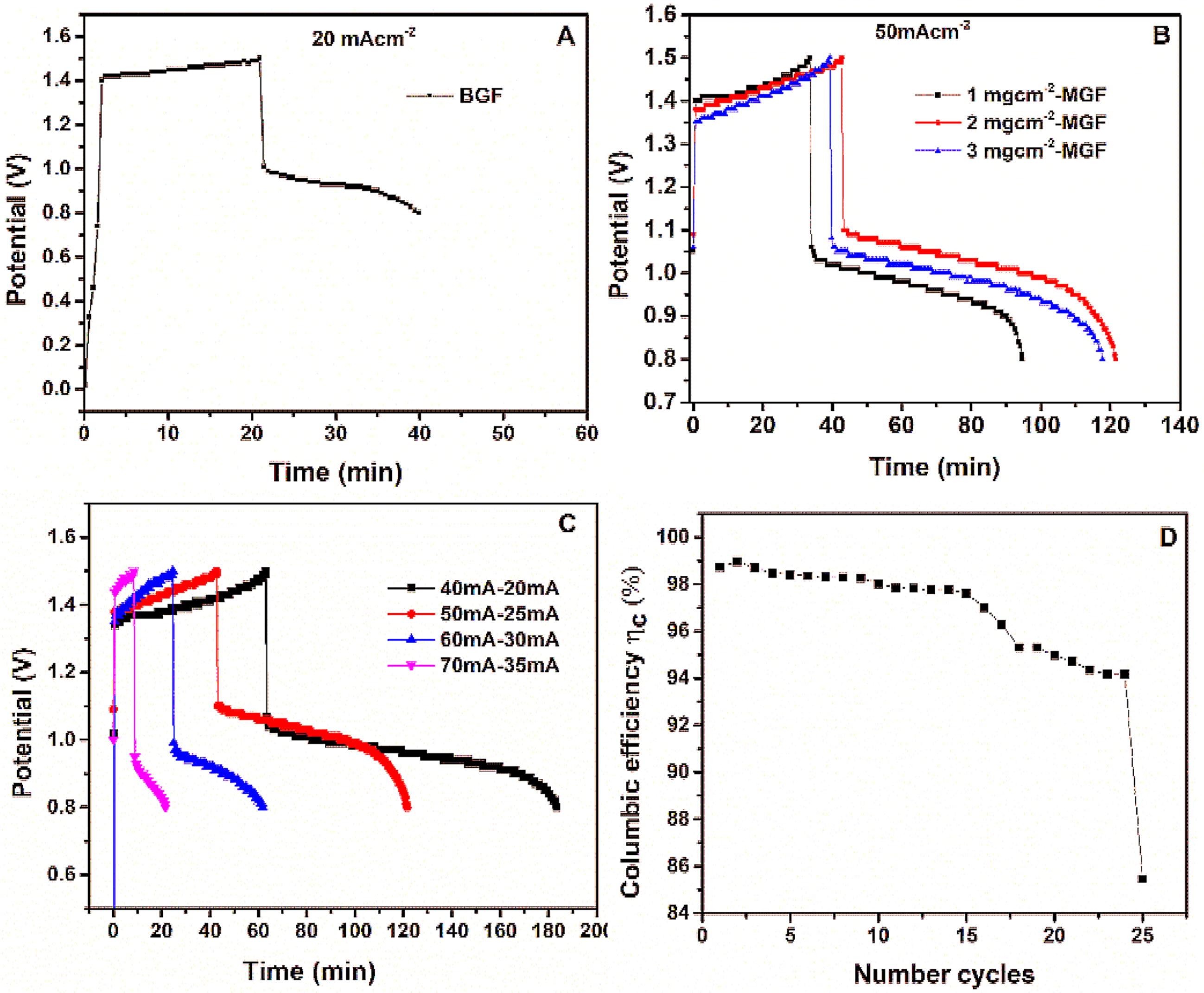

Fig. 8 Charge–discharge studies for **a** BGF (20 mA cm^{-2}), **b** MGF (50 mA cm^{-2}) electrodes, **c** 2 mg cm^{-2}-MGF electrode at 40–70 mA cm^{-2}, **d** η_C characteristics against number of cycles

Table 4 Battery performance characterization for BGF electrodes (20 mA cm^{-2}) and MGF electrodes (50 mA cm^{-2})

Electrode sample	Coulombic efficiency (η_C) %	Peak power density (PPD) mW cm^{-2}
BGF	44.36	11.51
1 mg cm^{-2}-GOMGF	91.53	46.59
2 mg cm^{-2}-GOMGF	98.96	55.60
3 mg cm^{-2}-GOMGF	94.77	48.40

Table 5 Battery performance characterization using 2 mg cm^{-2}-MGF electrode

Current densities (mA cm^{-2})	Coulombic efficiency (η_C) %	Peak power density (PPD) mW cm^{-2}
40	99.10	57.32
50	98.96	55.60
60	91.01	46.58
70	88.22	40.77

The η_C and PPD were between 88.22 and 99.10% and between 40.77 and 57.32 mW cm^{-2}, respectively (Table 5).

In addition, the stability of the cell was studied using 2 mg cm^{-2}-MGF electrode and the data were plotted for number of cycles Vs η_C as shown in Fig. 8d. The η_C for first cycle was found to be 98.74% which increases to 98.97% at second cycle, but decreases gradually and becomes 85.46% after the 25th cycle. The decrease in the η_C may be due to the loss of stability of electrolyte or saturation of the modified electrode (2 mg cm^{-2}-MGF). The average η_C and PPD of the cell after 25 cycles was found to be 96.06% and 55.56 mW cm^{-2}, respectively. At a current density of 70 mA cm^{-2}, η_C was 88.22%. The performance results provide good evidence of the stability of the MnO_2@CeO_2 composite-modified electrode.

Most of the reports on IRFBs use non-aqueous iron electrolytes with three-electrode systems and activation area lesser than 25 cm^2. Few studies also report aqueous iron electrolytes but mainly focus on ligand optimizations [33–37]. The performance of IRFBs were studied at different conditions and are compared in Table 6. The IRFBs reported have produced better efficiencies of 90–97% at much lower current densities ($\leq$ 10 mA cm^{-2}). The non-aqueous iron electrolytes used in the IRFBs systems are not economical and also pose a hazard to the environment. In this work, an effort has been made to demonstrate the cell (132 cm^2) with higher active area using modified electrode and optimized aqueous electrolyte. The 2 mg cm^{-2}-MGF electrode provided an efficiency of 98.96% (50 mA cm^{-2}) η_C as compared with BGF electrode (44.36%@20 mA cm^{-2}).

4 Conclusions

A simple hydrothermal process was used to synthesize the MnO_2@CeO_2 composite. Synthesized MnO_2@CeO_2 composites were used to modify GF electrode by electrostatic spraying after ultra-sonication. Performance characterization of BGF and MGF electrodes were studied using $FeCl_2$ as an electrolyte. At 50 mA cm^{-2}, the 2 mg cm^{-2}-MGF electrode exhibits good charge/discharge characteristics with a η_C of 98.96%. The 2 mg cm^{-2}-MGF electrodes had enhanced reversibility of the redox reaction and lower resistance in electrochemical studies, which is beneficial to obtain good results during the cyclic performance of IRFBs. The obtained performance was attributable to the unique morphology and oxygen moieties on surface properties. The modification of the GF electrode results in good efficiency and cyclic performance reveals that IRFBs are potentially feasible for grid-level energy storage.

Table 6 Performance characterization of various cells in iron electrolytes

Positive electrode	Electrolyte	Coulombic efficiency (η_C) (%)	Area of electrode cm^2	References
Iron rod	Iron(II) chloride, Iron(II) sulfate	97.0	1	[33]
Porous carbon paper	Iron(III) chloride, Iron(III) sulfate	90.0	10	[34]
[Glassy carbon]	Iron-triethanolamine, Iron-cyanide	93.0	–	[35]
Graphite rod	Iron-triethanolamine/bromide	82.4	0.103	[36]
Rotating disk glassy carbon	Iron(II) chloride,	97.0	25	[37]
Rayon graphite felt (2 mg cm^{-2}-MGF)	Iron(II) chloride	98.96	132	This study

Acknowledgements The authors gratefully thank the Department of Science and Technology (DST), India, for financial support under MES scheme 2016 ((Grant Number DST/TMD/MES/2k16/83)). We also thank the Centre for Incubation, Innovation, Research and Consultancy (CIIRC), Jyothy Institute of Technology and Sri Sringeri Sharadha Peetam for supporting this research.

Compliance with Ethical Standards

Conflict of interest H. B. Muralidhara, Centre for Incubation, Innovation, Research and Consultancy (CIIRC), Jyothy Institute of Technology, Thataguni, Off Kanakapura Road, Bangalore 560 082, Karnataka, India, has received research grants from Department of Science and Technology (DST), India. The authors declare that they have no conflict of interest.

References

1. C. Julien, A. Mauger, A. Vijh, k. Zaghib, Lithium batteries, (Springer,2016)
2. B. Li, M. Gu, Z. Nie, Y. Shao, Q. Luo, X. Wei, Nano Lett. **13**, 1330 (2013)
3. C. Liu, J. Yuan, R. Masse, X. Jia, W. Bi, Z. Neale, Z Adv. Mater. **1905245** (2020)
4. S. Xin, Y.X. Yin, Y.G. Guo, L.J. Wan, Adv. Mater. **26**, 1261 (2014)
5. M. Skyllas-Kazacos, M. Rychcik, R.G. Robins, A. Fane, M. Green, J. Electrochem. Soc. **133**, 1057 (1986)
6. E. Sum, M. Rychcik, M. Skyllas-Kazacos, J. Power Sources **16**, 85 (1985)
7. H. Jiang, Y. Zeng, M. Wu, W. Shyy, T. Zhao, Appl. Energy **240**, 226 (2019)
8. E. Sum, M. Skyllas-Kazacos, J. Power Sources **15**, 179 (1985)
9. X.W. Wu, Q. Deng, C. Peng, X.X. Zeng, A.J. Wu, C.J. Zhou, ACS Appl. Mater. Interface **11**, 11451 (2019)
10. T.M. Tseng, R.H. Huang, C.Y. Huang, C.C. Liu, K.L. Hsueh, F.S. Shieu, J. Electrochem. Soc. **160**, A690 (2014)
11. F.Q. Xue, Y.L. Wang, W.H. Wang, X.D. Wang, Electrochim. Acta **53**, 6636 (2008)
12. C. Flox, J. Rubio-Garcia, R. Nafria, R. Zamani, M. Skoumal, T. Andreu, Carbon **50**, 2372 (2012)
13. Y.C. Chang, J.Y. Chen, D.M. Kabtamu, G.Y. Lin, N.Y. Hsu, Y.S. Chou, J. Power Sources **364**, 1 (2017)
14. T.M. Tseng, R.H. Huang, C.Y. Huang, C.C. Liu, K.L. Hsueh, F.S. Shieu, J. Electrochem. Soc. **161**, A1132 (2014)
15. T.M. Marques, O.P. Ferreira, J.A. Da Costa, K. Fujisawa, M. Terrones, B.C. Viana, J. Phys. Chem. Solids **87**, 213 (2015)
16. M. Grünbacher, L. Schlicker, M.F. Bekheet, A. Gurlo, B. Klötzer, S. Penner, Phys. Chem. **20**, 22099 (2018)
17. A. Rajendran, S. Kandasamy, Mater. Res. Innov. **23**, 15 (2019)
18. R. Saravanan, S. Agarwal, V.K. Gupta, M.M. Khan, F. Gracia, E. Mosquera, J. Photochem. Photobiol. A. **353**, 499 (2018)
19. J. Papavasiliou, M. Rawski, J. Vakros, G. Avgouropoulos, ChemCatChem. **10**, 2096 (2018)
20. H. Zhang, J. Gu, J. Tong, Y. Hu, B. Guan, B. Hu, Chem. Eng. J. **286**, 139 (2016)
21. H. Zhou, J. Xi, Z. Li, Z. Zhang, L. Yu, L. Liu, RSC Adv. **4**, 61912 (2014)
22. M. Govindan, K. He, I.S. Moon, Int. J. Electrochem. Sci. **8**, 10265 (2013)
23. M.A. Rodrigues, A.C. Catto, E. Longo, E. Nossol, R.C. Lima, J. Rare Earth. **36**, 1074 (2018)
24. H. Lin, J. Hu, H. Rong, Y. Zhang, S. Mai, L. Xing, J. Mater. Chem. A. **2**, 9272 (2014)
25. X. Yan, L. Tian, M. He, X. Chen, Nano Lett. **15**, 6015 (2015)
26. H. Wang, W. Yang, X. Wang, L. Huang, Y. Zhang, S. Yao, Sensor Actuat B-Chem. **304**, 127389 (2020)
27. T. Chhabra, A. Kumar, A. Bahuguna, V. Krishnan, Vacuum **160**, 333 (2019)
28. Q. Zhou, L. Zhang, P. Zuo, Y. Wang, Z. Yu, RSC adv. **8**, 36161 (2018)
29. D. Kong, J. Luo, Y. Wang, W. Ren, T. Yu, Y. Luo, Adv. Funct. Mater. **24**, 3815 (2014)
30. Y. Chen, Y. Zhang, D. Geng, R. Li, H. Hong, J. Chen, X. Sun, Carbon **49**, 4434 (2011)
31. K.J. Kim, S.-W. Lee, T. Yim, J.G. Kim, J.W. Choi, J.H. Kim, Sci. Rep. **4**, 6906 (2014)
32. G.P. Ojha, B. Pant, S.J. Park, M. Park, H.Y. Kim, J. Colloid Interface Sci. **494**, 338 (2017)
33. K.L. Hawthorne, T.J. Petek, M.A. Miller, J.S. Wainright, R.F. Savinell, J. Electrochem. Soc. **162**, A108 (2015)
34. M.C. Tucker, A. Phillips, A.Z. Weber, ChemSusChem. **8**, 3996 (2015)
35. K. Gong, F. Xu, J.B. Grunewald, X. Ma, Y. Zhao, S. Gu, Y. Yan, ACS Energy Lett. **1**, 89 (2016)
36. Y. Wen, H. Zhang, P. Qian, H. Zhou, P. Zhao, B. Yi, Y. Yang, Electrochim. Acta 2006. **51**, 3769 (2006)
37. A.K. Manohar, K.M. Kim, E. Plichta, M. Hendrickson, S. Rawlings, S. Narayanan, J. Electrochem. Soc. **163**, A5118 (2016)